Interplay of bound states in the continuum empowers spectral-lineshape manipulation in all-dielectric metasurfaces

Qin-Ke Liu,[1] Xiao-Qing Luo,[1,*] Xiaofeng Xu,[1] Yan Li,[2] Weihua Zhu,[1] Zhiyong Chen,[1] W. M. Liu,[3] and Xin-Lin Wang[1,4]

[1]*Hunan Province Key Laboratory for Ultra-Fast Micro/Nano Technology and Advanced Laser Manufacture, School of Electrical Engineering, University of South China, Hengyang 421001, China*

[2]*School of Nuclear Science and Technology, University of South China, Hengyang 421001, China*

[3]*Beijing National Laboratory for Condensed Matter Physics, Institute of Physics, Chinese Academy of Sciences, Beijing 100190, China*

[4]*School of Mechanical Engineering, University of South China, Hengyang 421001, China*

(Received 14 October 2022; revised 17 May 2023; accepted 17 May 2023; published 30 May 2023)

The bound states in the continuum (BICs) in optical metasurfaces have latterly received prominent attention for their ultrahigh quality factors and the promise that they hold for realizing lowthreshold nanolasers, high-harmonic generation, and slow-light devices. In this scenario, the flexible tuning of the BIC is at the heart of multifunctional and tunable metadevices underpinning the central role in the modulation of optical spectral responses. Most BIC-inspired works are limited to single types of BICs modes only affected by the structural perturbation without tunable functionality, while different types of BIC modes have received little attention in manipulating the spectral line shapes in optical metasurface. Here, we show that the simultaneous generation and tailored interplay of two types of BIC modes can empower the realization of tailorable spectral lineshape manipulation in all-dielectric metasurfaces. In particular, the magnetic symmetry-protected BICs and accidental BIC result from the preserved reflection symmetry and geometrical parameter perturbation, respectively. The varied asymmetric parameters and the polarization angle of the incident light are responsible for the generation and interplay of the symmetry-protected and accidental quasi-BIC modes. Additionally, the interplaying quasi-BICs enable the implementation of the dual-wavelength passive optical switches throughout the related telecom bands, and can exhibit the tunable spectral features of different types of Fano resonances and EIT analog-based slow-light effect. These results could offer exploration potential for the development of multifunction and high-performance metadevices.

DOI: 10.1103/PhysRevB.107.205422

I. INTRODUCTION

Metasurfaces, as ultrathin artificial subwavelength nanostructures made up of arrays of nanoresonators, have received a lot of attention in the past decade due to their unique capability to manipulate the degree of freedoms of the electromagnetic waves, including phase, amplitude, polarization, and frequency [1–6]. Likewise, metasurfaces are easy to fabricate with modern techniques, compact, and can also be cascaded with additional optical system functionality. Compared to the plasmonic metasurfaces that suffer from intrinsic loss, the all-dielectric metasurfaces consisting of high refractive index and low-loss materials offer excellent advantages for metadevices [7,8]. It is important to point out that the all-dielectric metasurfaces not only support higher quality factors (Q factors), but also enable the excitation of electromagnetic multipole resonances [9], which has exhibited powerful capabilities in designing spectral lineshapes in the near-infrared and terahertz regimes [8,10]. Among them, the sharp asymmetric Fano resonance [11,12] and electromagnetic-induced transparency (EIT) [13], which unfold a narrow transparent window along with unusual lineshapes and steep dispersion, yield avenues for biosensing [14,15], low-threshold lasers [16,17], nonlinear optics [18,19], and so on.

The bound states in the continuum (BICs) that reside in a radiative continuum but do not suffer damping, proposed by Neumann and Wigner in the context of quantum mechanics [20], figure quite general wave phenomena with infinite Q factors in physics, in general, and optics, in particular. The physical mechanisms that result in the formation of a BIC, in principle, can be classified as the symmetry-protected BIC and accidental BIC [7,21]. The symmetry-protected BICs, existing at high-symmetry points of the momentum space, remain localized within the radiative continuum spectrum only if the related symmetry (e.g., the reflection or rotational symmetry) in the system is preserved, whereas accidental BICs can be tailored in reciprocal space via structural parameter perturbation, despite the symmetry of the system being unchanged. In practice, the implementation of BICs are often restricted to quasi-BICs that represent supercavity modes with ultrahigh Q factors near the BIC conditions, such that the quasi-BICs are commonly regarded as BICs. Recently, BICs have been shown to offer exciting prospects for strong light confinement and high Q-factor applications in all-dielectric metasurfaces [22–24], such as light manipulation [16,25,26], high-harmonic generation [27–30], and slow-light devices [31–33]. It has been demonstrated that the Q factor

*Corresponding author: xqluophys@gmail.com

of an isolated BIC is distinctly influenced by inevitable fabrication imperfections (such as inhomogeneity, finite sample size, and surface roughness of the metasurface) [7], thereby leading to the BIC mode coupling with the nearby radiative states, which restricts its practical applications. Moreover, most previous reported works that predominantly concentrate on the implementation of individual BIC or multiple isolated BICs are affected only by the structural perturbation without tunable functionality. Thus, these BICs are insufficient for the flexible manipulation of spectral lineshapes designing functional optical devices, while the tailored interplay of different types of BIC modes can be adapted to manipulate the spectral lineshapes and further adjust the Q factor of nearby radiative states, which also provides stability to fabrication imperfections. To effectively exploit the potential of the BICs in all-dielectric metasurfaces, the flexible tuning of the BIC promotes the exploitation of the multifunctional and tunable metadevices, which has not been well understood and requires further study.

In this paper, we show that the simultaneous generation of symmetry-protected BICs and accidental BIC as well as the customized interplay of these two types of BIC modes can empower the spectral lineshape manipulation for optical switches and tunable slow light effect in all-dielectric metasurfaces, which consists of periodic silicon square including circular-aperture (CA) and circular-hole (CH) unit cells. In particular, the symmetry-protected BICs and accidental BIC, dominated by magnetic multipoles and toroidal dipole (TD) responses, result from the preserved reflection symmetry and geometrical parameters perturbation, respectively. The varied asymmetric parameters and the polarization angle of the incident light are responsible for the generation and interplay of the symmetry-protected and accidental quasi-BIC modes while maintaining the accidental BIC. The interplaying quasi-BICs can be envisioned to facilitate the realization of dual-wavelength passive optical switches throughout the second and third telecom windows, and can exhibit the tunable spectral features of degenerate Fano resonance, double Fano resonances, and EIT analog-based slow-light effect by tuning polarization angle of the incident light. These results unveil the interplay of the BICs and show promise for the development of multifunction and high-performance metadevices such as tunable bandpass filters and multichannel sensing.

II. STRUCTURE AND MODEL

Herein, we consider an all-dielectric BIC-based silicon metasurface that consists of a periodic silicon square including a CA and CH unit cell, as shown in Fig. 1(a), deposited on a quartz substrate. The linear polarized incident light field that propagates along the positive Z direction is normal to the metasurface. The geometric parameters of the single unit cell are presented in Fig. 1(b). $R_1 = R_2 = 150\,\text{nm}$ depict the radii of CA and CH, respectively, with $W = 390\,\text{nm}$ being the distance of the circle centers. $H = 120\,\text{nm}$ and $L = 750\,\text{nm}$ denote the height and side length of the silicon square, respectively. $P_x = P_y = 900\,\text{nm}$ are the periodic lengths of the unit cell in X and Y directions, respectively. It has been demonstrated that metasurfaces with broken reflection symmetry structure (the breaking of the in-plane inversion symmetry of a unit cell) can give rise to the presence of the SP-BIC [34]. As shown in Fig. 1(c), by varying the radius (R_1) of the CA, the asymmetric parameter $\alpha = \Delta S/S$ can be derived and exploited for the realization of SP-QBIC, where the distance of the circle centers W is fixed. Moreover, the numerical simulation of the BIC-based silicon metasurfaces can be achieved by harnessing the three-dimensional finite-difference time-domain (3D-FDTD) method [35,36], where the dielectric constants of silicon and quartz are from Refs. [37,38] (where the extinction coefficient κ of silicon at 1300 nm–1500 nm is reducing from 2.7×10^{-10} to 1×10^{-13}). Therein, the perfectly matched layers that can render a reflectionless absorbing medium, which absorbs without any reflected electromagnetic waves at all frequencies and angles of incidence, are set as the boundary conditions on the front and back sides of the Z direction, whereas the X and Y directions of the BIC-based silicon metasurface are considered as the periodic boundary conditions that ensure the continuous distribution of media on the boundary.

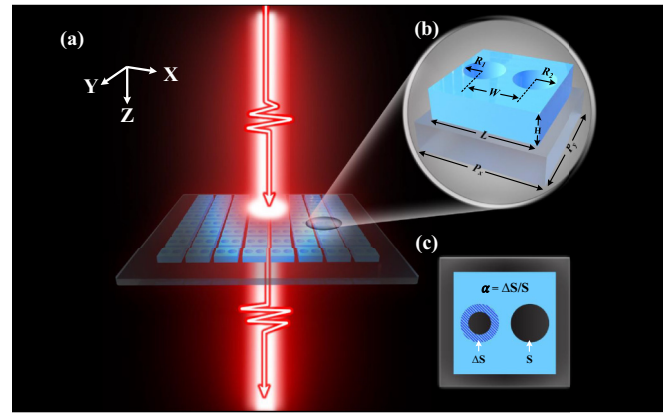

FIG. 1. (a) Schematic illustration of a BIC-based silicon metasurface consisting of circular-aperture (CA) and circular-hole (CH) unit cell deposited on a quartz substrate. The incident light acts vertically, along the positive Z direction, on the metasurface. (b) Side view of a unit cell with geometric parameters: R_1 and R_2 are the radii of CA and CH; W represents the distance of the circle centers; H and L denote the height and side length of the silicon square; P_x and P_y are the periodic length of the unit cell in X and Y directions, respectively. (c) Definition of the asymmetry parameter $\alpha = \Delta S/S$ for the silicon metasurface.

III. MAGNETIC SYMMETRY-PROTECTED BICS AND QUASI-BICS

It is known that a system that exhibits a reflection or rotational symmetry can enable the presence of the symmetry-protected BICs [39,40]. By slightly breaking one of the symmetries of the structure, the symmetry-protected BICs can be converted into symmetry-protected quasi-BICs resonance modes with an ultrahigh Q factor [41,42]. When the incident light is polarized along the Y direction, the reflection symmetry of the metasurfaces can be broken by varying the radius R_1 of the CA structure. As shown in Fig. 2(a), for the radius $R_1 = 170\,\text{nm}$, there exist triple Fano resonances in the transmittance spectrum (see the brown curve). As the radius

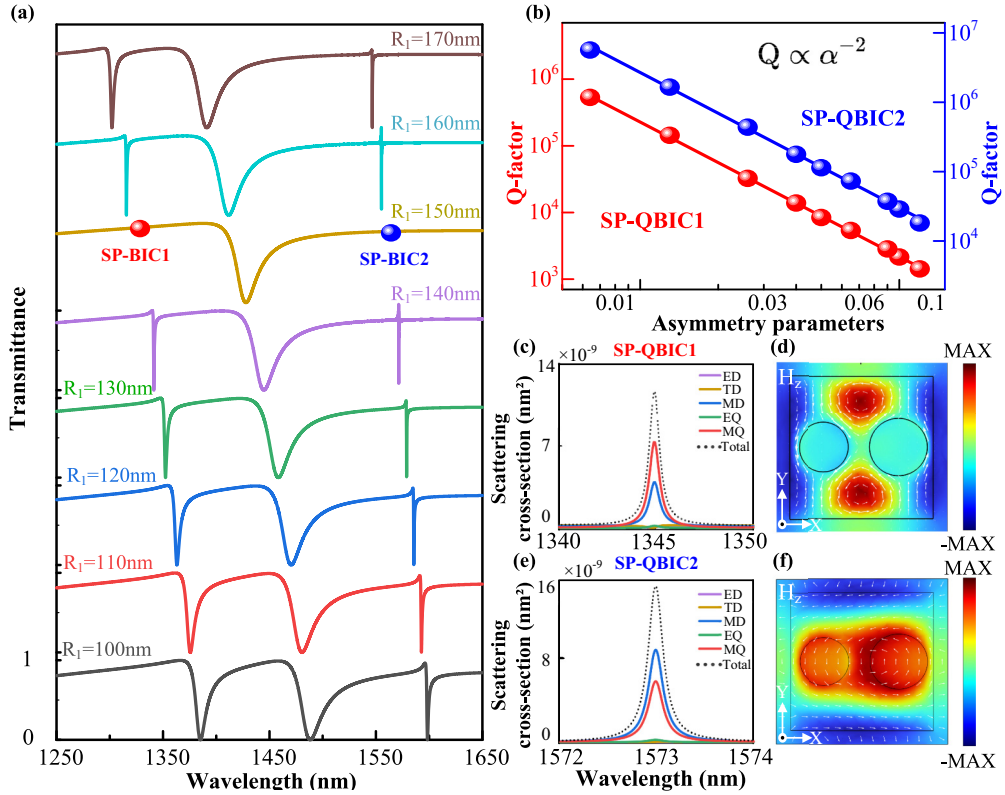

FIG. 2. Magnetic symmetry-protected BICs and quasi-BICs of the silicon metasurfaces. (a) Transmittance spectra with different radii R_1 of the CA structure. The red circle and blue triangle are marked as the symmetry-protected BIC1 (SP-BIC1) and BIC2 (SP-BIC2), respectively. (b) The Q factor of the two symmetry-protected quasi-BICs (SP-QBICs) with respect to different asymmetry parameters $\boldsymbol{\alpha}$, which agree well with $\mathbf{Q} \propto \boldsymbol{\alpha}^{-2}$. (c) The Cartesian multipole expansion of the scattering cross section of SP-QBIC1 and (d) the related intensity of the near-field magnetic field H_z in the X-Y plane on the metasurface for the radius $R_1 = 130$ nm (black arrows are displacement currents). (e) The Cartesian multipole expansion of the scattering cross section of SP-QBIC2 and (f) the related intensity of the near-field magnetic field H_z of the metasurface in the X-Y plane.

R_1 decreases from 170 nm to 100 nm, the center wavelengths of the triple Fano resonances are redshifted due to the increase of the effective refractive index of each unit cell, while the linewidth first decrease and then increase. For the radius $R_1 = 150$ nm (that is, reflection symmetry in the Y direction), two of the triple resonance modes vanish, which indicates that the external radiation channels of the bound state are closed, viz., no leaky energy to the free space. This process confirms the existence of the two symmetry-protected BICs (see the red circle and blue triangle for the SP-BIC1 and the SP-BIC2, respectively), which can also be verified from the band structures and Q factor of these two nonradiative modes (see more details in Fig. 7 of the Appendix). Moreover, the breaking of the reflection symmetry results in the presence of symmetry-protected quasi-BIC1 (SP-QBIC1) and quasi-BIC2 (SP-QBIC2), namely, dubbed supercavity modes. Therein, both the Q factor and resonance linewidth become finite. To evaluate the effect of the symmetry breaking on SP-QBIC1 and SP-QBIC2, the asymmetry parameters ($\boldsymbol{\alpha}$) are introduced to analyze the scaling behavior of the quality factor (Q factor). The Q factor is defined as $\lambda_0/\Delta\lambda$, with λ_0 being the resonant wavelength and $\Delta\lambda$ being the full width at half maximal of the resonance. It is found that the Q factor of both the SP-QBIC1 and SP-QBIC2 modes are obviously proportional to $Q \propto \alpha^{-2}$, as shown in Fig. 2(b), which, in turn, validates the existence of the symmetry-protected BICs and quasi-BICs mentioned above. It should be noted that the silicon absorption loss can be ignored in the calculation of the Q factors of the two SP-QBIC modes, thus fitting well with the α^{-2} and exhibiting an ideal SP-BIC with infinite value of the Q factors. In Fig. 2(c), the Cartesian multipole expansion of the far-field scattering cross section of the SP-QBIC1 is dominated by the magnetic quadrupole (MQ) with the magnetic dipole (MD) being secondary contributions, which can also be verified by the magnetic field distribution in Fig. 2(d). Nevertheless, as shown in Fig. 2(e), the Cartesian multipole expansion of the far-field scattering cross section of the SP-QBIC2 is governed by the MD with the MQ being secondary contributions, which can also be verified by the magnetic field distribution in Fig. 2(f). The results reveal that the symmetry-protected BICs and quasi-BICs are mainly attributed to the magnetic responses, while the electric responses are nearly suppressed, which also make them attractive for biosensors of superior sensitivity and detectability [43,44].

IV. TOROIDAL-DIPOLE-BASED ACCIDENTAL BIC AND QUASI-BIC

In the previous subsection, the magnetic symmetry-protected BICs and quasi-BICs were realized by considering

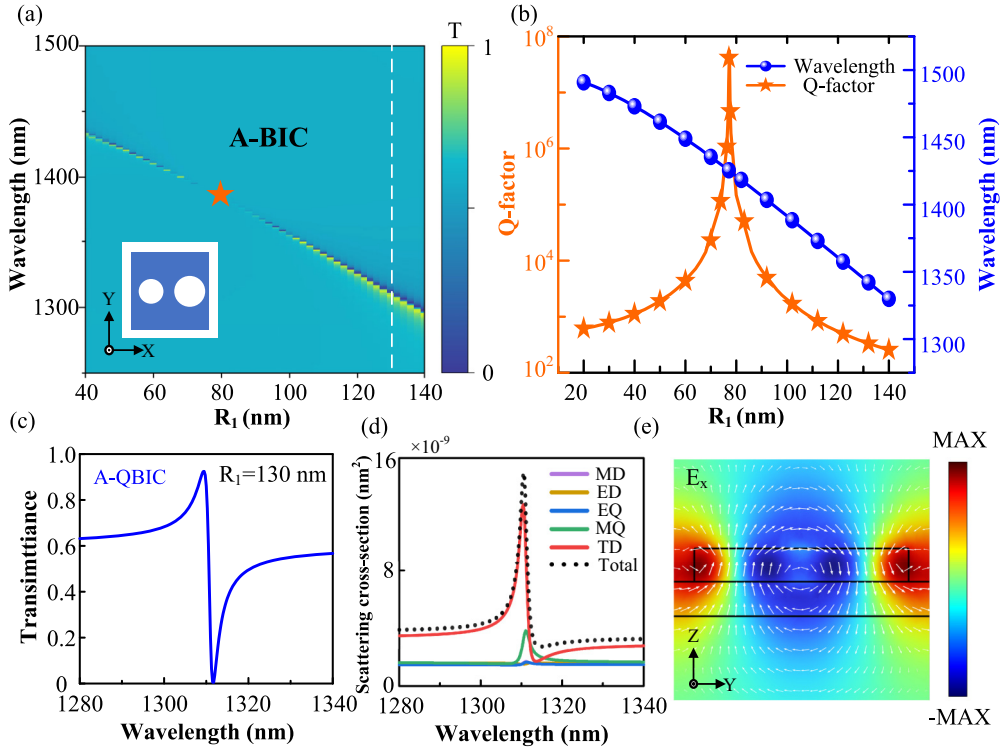

FIG. 3. Toroidal-dipole-based accidental BIC and quasi-BIC as the incident light polarized along the X direction. (a) The transmittance spectra as a function of R_1 and the wavelength. The toroidal-dipole-based accidental-BIC (A-BIC) is marked with an orange pentagram. (b) Dependence of the Q factor and resonance wavelength of the accidental quasi-BIC (A-QBIC) on different R_1. (c) The transmittance spectrum of the metasurface at $R_1 = 130$ nm [see the vertical white dashed line in (a)], exhibits an asymmetric Fano lineshape. (d) The Cartesian multipole expansion of the scattering cross section of A-QBIC in (c). (e) The electromagnetic near-field distribution in the Y-Z plane with X direction corresponding to the near half length of the circle centers ($\lambda = 1310$ nm). The contour plot represents the near-field electric distribution E_x, while the white arrow and its length indicate the direction and magnitude of the magnetic field, respectively.

the reflection symmetry and asymmetry of the metasurface, respectively, when the incident light was polarized along the Y direction. By fixing the polarized direction of the incident light at the X direction, albeit with varied radius R_1, the reflection symmetry is always preserved. As shown in Fig. 3(a), the transmittance spectra accidentally vanish by changing the radius R_1, which demonstrate that the existence of the accidental BIC (A-BIC), marked with an orange pentagram, can be evolved from accidental quasi-BIC (A-QBIC) [45], while the band structures and Q factors of the eigenmode near the first Brillouin zone also confirm the existence of A-BIC (See more details in Fig. 7 of the Appendix). As shown in Fig. 3(b), the resonance wavelengths are blueshifted continuously by increasing the radius R_1 (see the blue-circle curve), owing to the diminishing of the effective refractive index of the metasurface. The Q factor first exponentially increases and then exponentially decreases along with a maximal point that delineates the A-BIC by increasing the radius R_1 (see the orange pentagram curve)—herein, as mentioned in Fig. 2(b), the ideal A-BIC with infinite Q factor. The transmittance spectrum of the metasurface at $R_1 = 130$ nm [see the vertical white dashed line in Fig. 3(a)], exhibits an asymmetric Fano lineshape in Fig. 3(c), indicating that the radiating source weakly interacts with the free space, and then significantly reduces the radiative loss in the metasurface. As illustrated in Fig. 3(d), the Cartesian multipole expansion of the far-field scattering cross section of the A-QBIC shows that the TD plays the key role in all of the multipole modes [46], where the MQ and electric quadrupole (EQ) are successive contributions. Such behaviors can also be verified by the electromagnetic field distribution in Fig. 3(e). Therein, a TD is dominated by either a counterclockwise toroidal magnetic field (which ranges from A-QBIC to A-BIC, i.e., the radius is less than 78 nm) or a neighboring clockwise toroidal magnetic field (which ranges from A-BIC to A-QBIC, to wit, the radius is more than 78 nm) formed in the Y-Z plane. As a consequence, the TD-based A-BIC and A-QBIC can be fulfilled by varying the radius R_1 of the CA of the metasurface.

V. MANIPULATING THE INTERPLAY OF TWO TYPES OF BIC MODES

The previously specified SP-BIC and A-BIC modes that suffer from different polarized incident light have many potential applications in low-threshold room-temperature lasing [17,47], biosensors [48,49], and so on, due to their ability to enhance light-matter interactions, which is fundamental to increase the efficiency and improve the performance of the nanophotonic devices. As shown in Fig. 4(a), by fixing $R_1 = 130$ nm, the SP-QBIC1 and A-QBIC present at 1340 nm and 1310 nm, respectively, when the polarization angle of the incident light changes from 0° to 90°. The SP-QBIC1

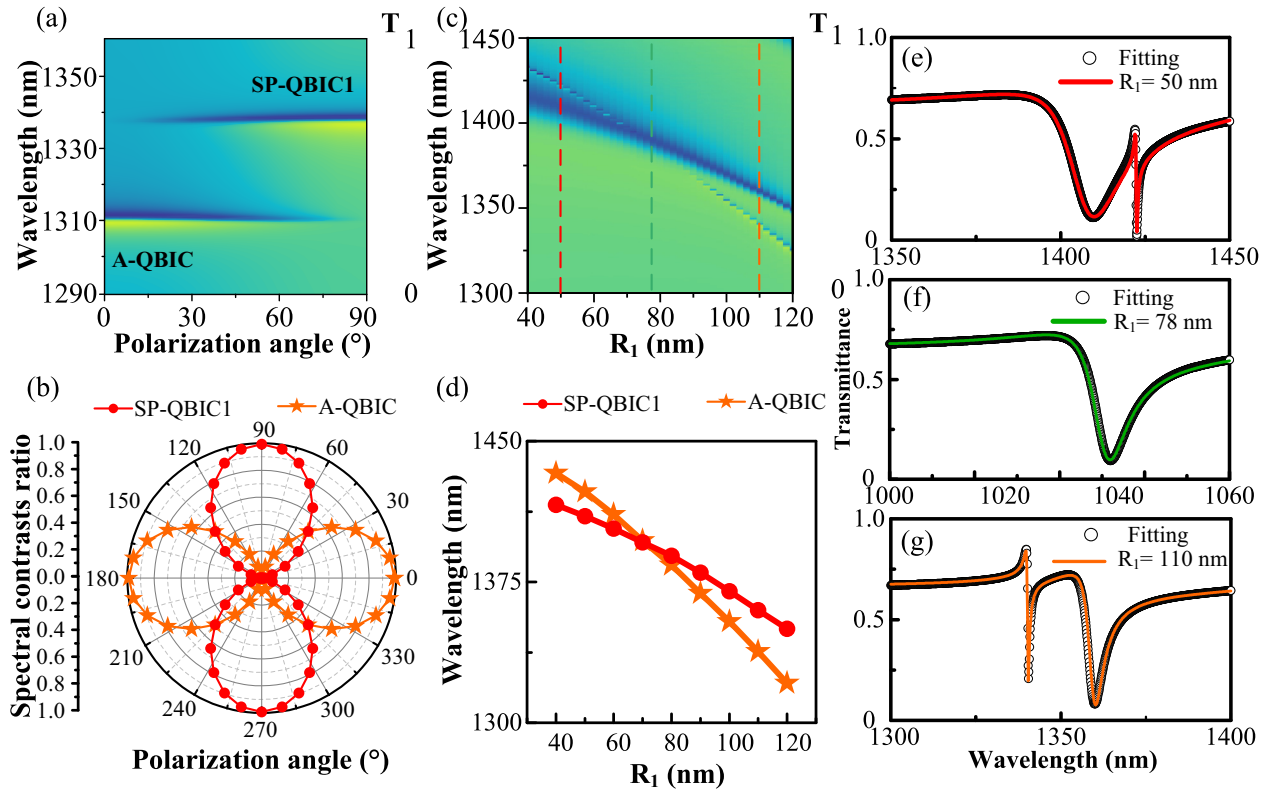

FIG. 4. The polarization-selective excitation and interplay of the SP-QBIC1 and the A-QBIC. (a) Transmittance spectra with different wavelengths and polarization angles. (b) Spectral contrast ratios of the SP-QBIC1 and the A-QBIC with different polarization angles. (c) Transmittance spectra as a function of the wavelength and radius R_1, with the polarization angle being fixed at 45°. (d) The resonance wavelengths of the SP-QBIC1 and the A-QBIC with different radius R_1 in (c). (e)–(g) The transmittance spectra and MICMT fitting with fixed radius R_1, which corresponds to the red, green, and orange vertical dashed lines in (c), respectively.

and A-QBIC modes vanish as the polarization angles near 0° and 90°, respectively. This behavior can be ascribed to the polarization-selective modulation of supercavity resonances using subwavelength aperture arrays. It has already been demonstrated that the Poincaré sphere can visually illustrate the polarization state of the incident light, and is a general way to exhibit the degree of polarization of the linearly and circularly polarized light [50–52]. In our scheme, only one of the longest axes (the equatorial axis) of the Poincaré sphere can be used to illustrate the degree of polarization of the linearly polarized light (only S_1 and S_2 axes exist to form a circular plane), which is similar to the in-plane polar plots. The spectral contrasts ratios of the SP-QBIC1 and A-QBIC modes in Fig. 4(b), defined as $[(T_{\text{peak}} - T_{\text{dip}})]/[(T_{\text{peak}} + T_{\text{dip}})] \times 100\%$ with T_{peak} and T_{dip} being the maximum and minimum of the transmittance spectra [53], can be used to quantify the degree of polarization-selective excitation. Therein, for the A-QBIC (SP-QBIC1), the maximum (minimum) excitation appears at both 0° and 180° with the contrast ratios being close to 100% (0), while the minimum (maximum) excitation occurs at 90° and 270° with the contrast ratios being close to 0 (100%). It is of great interest to notice that, for the polarization angle being 45° (135°, 225°, and 315°), the SP-QBIC1 and A-QBIC modes are identically excited at this moment, resulting from the equivalent electric field components of the incident light in the X and Y directions. Subsequently, by fixing the polarization angle at 45°, the interplay of the SP-QBIC1 and the A-QBIC can be realized by regulating the radius R_1 in Fig. 4(c), which can also be verified from the change of the resonance wavelengths in Fig. 4(d).

Furthermore, the underlying physical mechanisms of the interplay of two types of BIC modes can be validated by using the multimode interference coupled mode theory (MICMT), which has been extensively conducted to explain the physical origin of the Fano resonance and multiple Fano resonances [54,55]. With respect to the coupled multiple resonant modes, the coupling phases of different resonant modes have a profound impact on their transmittance spectra. From the single-mode coupled-mode-theory, the basic equations of the MICMT with coupling phases can be given as

$$S_{n,1}^{+} = \gamma_{n1} e^{i\varphi_{n1}} S_1^{+}, \quad S_{n,2}^{+} = \gamma_{n2} e^{i\varphi_{n2}} S_2^{+}, \tag{1}$$

$$S_1^{-} = -S_1^{+} + \sum_n \kappa_{n1}^{*} a_n, \quad \kappa_{n1} = \sqrt{\frac{2}{\tau_{n1}}} e^{i\theta_{n1}}, \tag{2}$$

$$S_2^{-} = -S_2^{+} + \sum_n \kappa_{n2}^{*} a_n, \quad \kappa_{n2} = \sqrt{\frac{2}{\tau_{n2}}} e^{i(\theta_{n1} - \phi_n)}, \tag{3}$$

$$\frac{da_n}{dt} = \left(-i\omega_n - \sum_{k=0}^{2} \frac{1}{\tau_{nk}}\right) a_n + \kappa_{n1} S_1^{+} + \kappa_{n2} S_2^{+}, \tag{4}$$

where $S_k^{\pm} (k = 1, 2)$ are the field amplitudes for the outgoing $(-)$ and incoming $(+)$ ports of 1 and 2, respectively.

$\gamma_{n1}e^{j\varphi_{n1}}$ and $\gamma_{n2}e^{j\varphi_{n2}}$ denote the normalized coefficients ($\gamma_{n1} = \gamma_{n2} \approx 1$ in this paper). φ_n represents the phase difference between outgoing and incoming ports of the nth resonant mode. θ_{nk} and κ_{nk} $(k = 1, 2)$ depict the phases and coupling coefficients of the nth resonant mode, respectively, with κ^*_{nk} $(k = 1, 2)$ being the related complex conjugate terms of the coupling coefficients. ϕ_n indicates the phase difference between the outgoing and incoming ports of the nth resonant mode. a_n and ω_n are the field amplitude and resonant frequency of the resonant mode, respectively. τ_{n0} is the decay time of internal loss of the nth resonant mode in resonator. τ_{n1} and τ_{n2} are the decay time of the coupling between the resonator and environment, respectively. For the single-incoming case, by setting S_2^+=0, the transmittance of the metasurface can be written as

$$T = \left|\frac{S_2^-}{S_1^+}\right|^2 = \left|t_0 + \sum_{n=1}^{N} \frac{2\tau_{n0}e^{i\varphi_n}}{-i(\omega-\omega_n)\tau_n\tau_{n0} + 2\tau_{n0} + \tau_n}\right|^2, \tag{5}$$

where φ_n denotes the total coupling phase difference for the SP-QBIC1, A-QBIC, and a Fano-type resonant (peak at $\lambda = 1490$ nm) mode. t_0 delineates a constant that compensates the other resonances in the uninterested frequency range as a flat continuous background. In Figs. 4(e) and 4(f), the MICMT agrees well with the numerical results. For the radius $R_1 = 50$ nm [see the red curve in Fig. 4(e)] and $R_1 = 110$ nm [see the orange curve in Fig. 4(f)], the interplay of the SP-QBIC1 (that is the supperradiant mode with low Q factor) and A-QBIC (that is the subradiant mode with high Q factor) can be realized by adjusting the radius R_1. It should be noted that, for the radius $R_1 = 78$ nm [see the green curve in Fig. 4(f)], the SP-QBIC1 is preserved, while the A-QBIC is transformed to A-BIC. The fitting parameters of the interplay of two types of BIC modes are given as follows: (e) $N = 3$, $t_0 = 0.8$, $\omega_1 = 2.1077 \times 10^{14}$ rad/s, $\omega_2 = 2.1307 \times 10^{14}$ rad/s, $\omega_3 = 2.0120 \times 10^{14}$ rad/s, $\tau_{10} = 69920$ fs, $\tau_{20} = 1702$ fs, $\tau_{30} = 2721$ fs, $\tau_1 = 911002.1$ fs, $\tau_2 = 3080.7$ fs, $\tau_3 = 8104.6$ fs, $\varphi_1 = -2.25$, $\varphi_2 = 0.41$, and $\varphi_3 = -2.4$. (f) $N = 3$, $t_0 = 0.795$, $\omega_1 = 2.1845 \times 10^{14}$ rad/s, $\omega_2 = 2.1599 \times 10^{14}$ rad/s, $\omega_3 = 2.0202 \times 10^{14}$ rad/s, $\tau_{10} = 1730000$ fs, $\tau_{20} = 2410$ fs, $\tau_{30} = 1520$ fs, $\tau_1 = \infty$, $\tau_2 = 3976.6$ fs, $\tau_3 = 4304.6$ fs, $\varphi_1 = -2.25$, $\varphi_2 = 0.41$, and $\varphi_3 = -2.5$. (g) $N = 3$, $t_0 = 0.795$, $\omega_1 = 2.2367 \times 10^{14}$ rad/s, $\omega_2 = 2.2060 \times 10^{14}$ rad/s, $\omega_3 = 2.0534 \times 10^{14}$ rad/s, $\tau_{10} = 39920$ fs, $\tau_{20} = 5300$ fs, $\tau_{30} = 1525$ fs, $\tau_1 = 91000.3$ fs, $\tau_2 = 7976.5$ fs, $\tau_3 = 4304.6$ fs, $\varphi_1 = -2.5$, $\varphi_2 = 0.45$, and $\varphi_3 = -2.45$. These results elucidate that, by modulating the radius R_1 of the CA of the metasurface, the polarization-sensitive SP-QBIC1 and A-QBIC are capable of interplay with each other while simultaneously sustaining the A-BIC.

VI. QUASI-BIC-BASED PASSIVE DUAL-WAVELENGTH OPTICAL SWITCHES

It is typically found that metasurface-based optical switches have great potential for applications in optical logic circuits and optical communication systems [56–58]. Among them, integration of passive optical switching devices with optical fibers benefit the implementation of practical applications in long-distance optical data transmission, optical remote sensing, and all-optical networks [59,60]. In view of the fact that the all-dielectric metasurface is very favorable for improving the performance of optical switches due to its resonant internal field localization and low energy dissipation, in this respect we explore the passive dual-wavelength optical switches in the all-dielectric BIC-based silicon metasurface. As shown in Fig. 5(a), for the central wavelengths of 1482 nm and 1487 nm [which pertains to the telecom S-band (1460−1530 nm)], their transmittance spectra can be adjusted by varying the orientation of the incident polarization, where the maximal and minimal of the transmittances can be installed as the ON and OFF states of the optical switches, respectively. Hence, the ON/OFF ratio η can be defined as [60]

$$\eta = 10\log_{10}\left(\frac{T_{ON}}{T_{OFF}}\right), \tag{6}$$

where T_{ON} and T_{OFF} depict the ON and OFF states at the related wavelengths, respectively. As indicated by Fig. 5(b), with regard to the center wavelength at 1483 nm, the ON state of the optical switch, induced by the SP-QBIC1 mode, can be acquired with the transmittance being $T_{ON} = 0.921701$, when the incident polarized along the Y-direction (i.e., the polarization angle is 90°). Simultaneously, the OFF state of the optical switch, triggered by the A-BIC mode, can be achieved with the transmittance being $T_{OFF} = 0.0000133$, when the incident polarized along the X direction (i.e., the polarization angle is 0°). Then, the ON/OFF ratio η of the center wavelength (1483 nm) can be attained as 48.4 dB. For the case of the center wavelength at 1487 nm, the ON state of the optical switch, triggered by the *peak* of the A-BIC mode, can be achieved with the transmittance being $T_{ON} = 0.471216$, when the incident is polarized along the X direction (0°). While the OFF state of the optical switch, induced by the *dip* of the SP-QBIC1 mode, can be obtained with the transmittance being $T_{OFF} = 0.00004366$, when the incident is polarized along the Y direction (0°). Thus, the ON/OFF ratio η of the peak-dip-type optical switch at 1487 nm can be attained as 40.3 dB. Of particular interest is that the dual-wavelength optical switches, as illustrated in Fig. 5(c), can be ranged throughout the second and third telecom windows by changing the side length (L) of the silicon square, with the ON/OFF ratio η ranging from 34 dB to 48.4 dB, respectively. These results illustrate that the quasi-BICs based dual-wavelength passive optical switches can be accomplished in the telecom S-band with high ON/OFF ratios, and can be extended throughout the second and third telecom windows. Such dual-wavelength optical switches, which are compact and passive devices without adding additional active pump light field, is promising to enrich the applications in optical communication and all-optical computing devices [57,61].

VII. TUNABLE SLOW LIGHT INDUCED BY THE INTERPLAY OF THE QUASI-BICS

It has been recently demonstrated that the high Q-factor quasi-BIC mode that is accompanied by a steep phase dispersion in an all-dielectric metasurface shows promising potential for practical applications in sensors [22], modulators

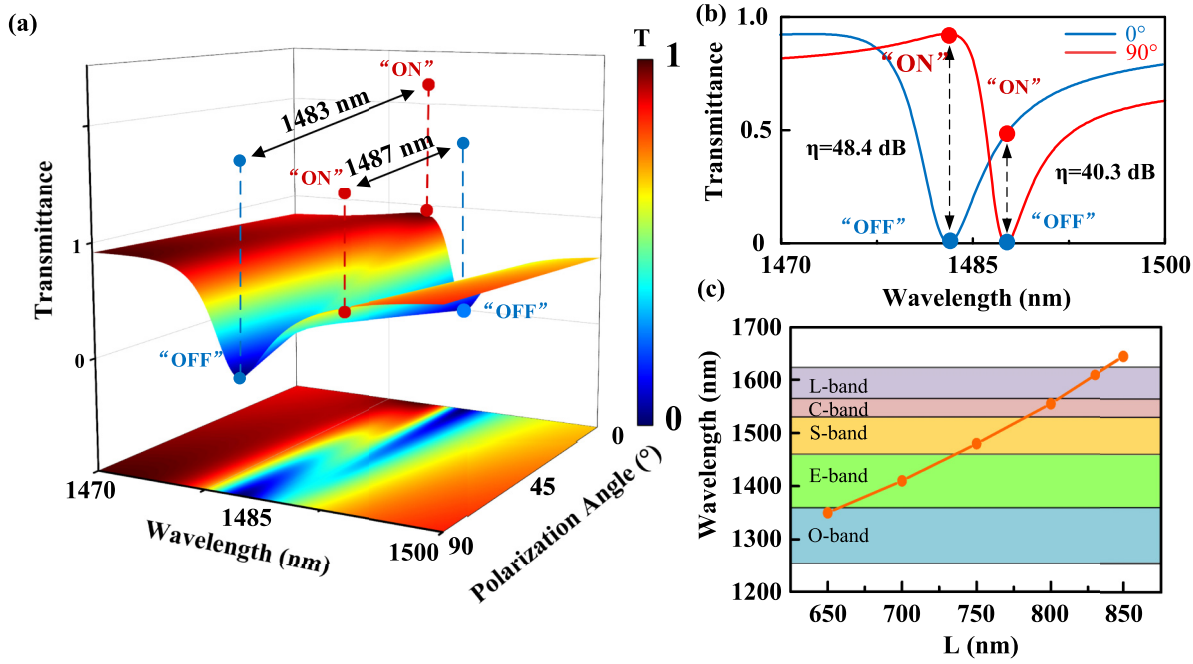

FIG. 5. Polarization-dependent passive dual-wavelength optical switches induced by SP-QBIC1 and A-QBIC. (a) The 3D surface-color map with projection of the dual-wavelength optical switches versus different wavelength and polarization angles of the incident light, where the resonance wavelengths are 1483 nm and 1487 nm with $R_1 = 34$ nm and $R_2 = 115$ nm, respectively. (b) The dual-wavelength optical switches operate at the telecom S-band (1460 − 1530 nm) with the ON/OFF ratio (η) being 48.4 dB and 40.3 dB, respectively. (c) The dual-wavelength optical switches can be ranged throughout the second and third telecom windows by changing the side length (L) of the silicon square.

[62], and slow-light devices [31,63]. The tunable slow-light effect in all-dielectric metasurfaces in the near-infrared region is particularly crucial to the various functional integrated photonic devices, e.g., all-optical buffers and all-optical switches [64,65]. Below we study the tunable slow-light effect induced by the interplay of the SP-QBIC1 and the A-QBIC. As shown in Fig. 6(a), by reducing the radius R_2 of CH to 115 nm [compared with the results shown in Fig. 4(c) with the radius R_2 being 150 nm], both the SP-BIC1 and A-BIC can be achieved near 1030 nm by varying the radius R_1 of CA, with the polarization angle of the incident light being fixing at 45°. In particular, for the radius R_1 being 36 nm and 58 nm, the transmittance spectra are characterized by *EIT analogs* [see the light blue curve in Fig. 6(b) and red curve in Fig. 6(d)], respectively, which are induced by the coherent interaction of the SP-QBIC1 and the A-QBIC. For the radius R_1 being 90 nm, the transmittance spectrum are portrayed as *double Fano resonances* [see the brown curve in Fig. 6(e)], resulting from the dipolar coupling of the SP-QBIC1 and the A-QBIC. Interestingly, it can be seen that, concerning the radius R_1 being 46 nm, the transmittance spectrum obviously features the single Fano resonance [see the orange curve in Fig. 6(c)], which originates from the degenerate dipolar coupling of the SP-QBIC1 and the A-QBIC and can be termed as *degenerate Fano resonance* [66]. With respect to the EIT-like transmittance (the radius R_1 is 58 nm), we further show that the transmittance spectra evolve from polarization-selective Fano resonance to EIT analogs, and then to the orthogonal Fano resonance by altering the polarization angle of the incident light in Fig. 6(f). For the sake of studying the tunable slow-light effects govern by the EIT analogs, we explore the polarization angle on the group index (N_g) of the incident light in Fig. 6(g), which can be given as [65]

$$N_g = \frac{c}{v_g} = \frac{c}{D} \times \tau_g = -\frac{c}{D} \times \frac{d\varphi(\omega)}{d\omega}, \tag{7}$$

where c represents the speed of light in vacuum, D is the propagation distance of light in the metasurface, τ_g denotes the optical delay time, ω depicts the angular frequency, with $\varphi(\omega)$ being the phase shift of the transmittance. Thus, the positive group index, namely, inheriting the reduced group velocity, renders the appearance of the slow light. As illustrated in Fig. 6(g), it is obvious that the maximal group index 1911 (852) appears nearly at 1442 nm (1447 nm) with the polarization angle being 0° (90°). Also, the slow-light effect incurred by the EIT analog can be extended to the telecom bands by varying the side length (L) of the silicon square. Therefore, the interplay of the SP-QBIC1 and the A-QBIC can give insight into the realization of tunable slow-light effect with the high group index.

VIII. DISCUSSIONS AND CONCLUSIONS

As for the feasibility of the experimental setup, plasma-enhanced chemical vapor deposition [67], which has been widely used for the deposition of inorganic dielectric layers (such as nitride, silicide) due to the advantages of lower working temperature, faster deposition rate, and denser film layer, are conducted to deposit amorphous silicon films on quartz substrates. In doing so, not only the thickness of the

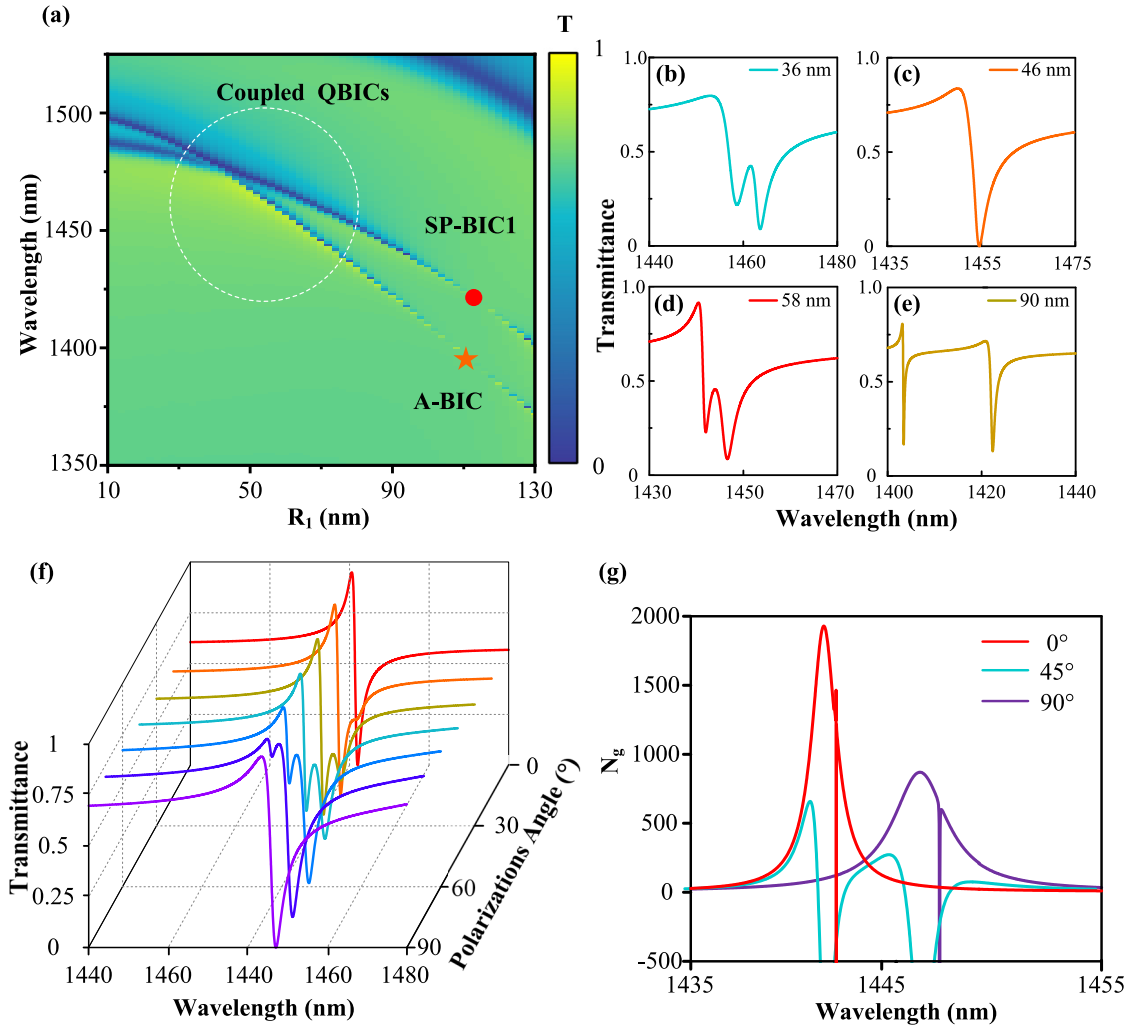

FIG. 6. Tunable slow-light induced by the interplay of the SP-QBIC1 and the A-QBIC. (a) The transmittance spectra of the coupled SP-QBIC1 and A-QBIC as a function of the wavelength and the radius R_1, with the polarization angle of the incident light being 45° and the radius $R_1 = 115$ nm. (b)–(e) The coupled quasi-BICs [zoomed view of the given range in the white-dashed circle in (a)] can be constructed as *EIT analogs* ($R_1 = 36$ nm and 58 nm), *degenerate Fano resonance* ($R_1 = 46$ nm), and *double Fano resonances* ($R_1 = 90$ nm), respectively. (f) Transmittance spectra as a function of the wavelength and polarization angle with the radius $R_1 = 58$ nm. (g) Tunable slow light with the group index induced by the polarization angle.

amorphous silicon film can be obtained by using the ellipsometry but the silicon square with CA and CH patterns can be carried out by electron-beam-lithography [68,69]. Thereafter, the related patterns can be transferred to the silicon film by reactive ion etching inductively coupled plasma with CHF_3, SF_6, Ar, and O_2 gases [70], thus leading to the realization of the BIC-based silicon metasurface. With regarding to the feasibility of the experimental measurement, a home-built optical system are used. After two fiber collimators are used to guide the optical path, the picosecond pulsed incident light is normal to the fabricated sample, and then the transmitted light can be collected by using a charge-coupled device detector in a time domain spectroscopy system. Meanwhile, the polarization direction of the incident light can be modulated by utilizing the polarization controller, resulting in the optical switch, and group delay of the incident light can be controlled by modulating the polarized direction of the incident light. As a consequence, the proposed all-dielectric BIC-based metasurface can be fabricated and the optical switch and slow-light effects are feasible to be observed in the experiment.

In summary, we have revealed that the generation and interplay of two types of BICs are capable of empowering spectral lineshape manipulation in all-dielectric silicon metasurfaces. It is shown that the symmetry-protected BICs and quasi-BICs stem from the MD and MQ responses, respectively, while the accidental BIC and quasi-BIC arise from the TD responses. Furthermore, the interplay of the symmetry-protected quasi-BIC and accidental quasi-BIC can be achieved while maintaining the accidental BIC, which is in good agreement with the MICMT. The interplaying quasi-BICs cannot only be employed for establishing the dual-wavelength passive optical switches in the telecom S-band or even throughout the second and third telecom windows but can be exploited for the realization of degenerate Fano

resonance, double Fano resonances, and EIT analog-based slow-light effects by tuning the polarization angle of the incident light. Therefore, our findings are promising for applications in metasurface-based devices including lowthreshold nanolasers, tunable bandpass filters, and biosensors.

ACKNOWLEDGMENTS

X.-Q.L. acknowledges support by the National Natural Science Foundation of China (Grant No. 12104214). W.-M.L. acknowledges support by the National Key Research and Development Program of China under Grants No. 2021YFA1400900, No. 2021YFA0718300, and No. 2021YFA1402100, National Natural Science Foundation of China under Grants No. 61835013, No. 12174461, and No. 12234012, Space Application System of China Manned Space Program.

APPENDIX: THE *Q* FACTOR AND BAND STRUCTURE OF THE SILICON METASURFACE

To further confirm the properties of the BIC modes, we analyze the eigenmodes and *Q* factors of the silicon metasurface by using the eigenfrequency solver of COMSOL Multiphysics, wherein the X and Y directions of the silicon metasurface are set as the Floquet periodic boundary conditions with the Z direction being considered as the perfect matching layer. As shown in Figs. 7(a) and 7(b), the eigenfrequencies of the A-BIC, SP-BIC1, and SP-BIC2 modes present near the first Brillouin zone (Γ point, along the *M*-Γ-*X* direction), respectively. The *Q* factors of the A-BIC, SP-BIC1, and SP-BIC2 modes, as shown in Figs. 7(c) and 7(d), diverge to infinity at Γ point. These behaviors indicate the nature of the BIC modes [39,45].

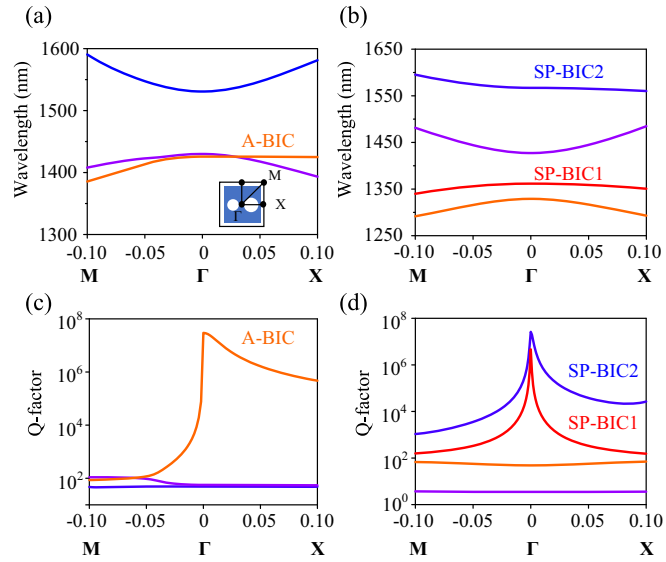

FIG. 7. The eigenmodes and factor of three BIC modes (the related solid orange, red, and blue lines). (a), (b) Simulated band structures correspond to the A-BIC, SP-BIC1, and SP-BIC2 with the eigenmodes of the metasurface near the Γ-point, respectively. (c), (d) Simulated *Q* factor of the eigenmodes correspond to the A-BIC, SP-BIC1, and SP-BIC2 near the Γ-point, respectively.

[1] A. I. Kuznetsov, A. E. Miroshnichenko, M. L. Brongersma, Y. S. Kivshar, and B. L. Yanchuk, Optically resonant dielectric nanostructures, Science **354**, aag2472 (2016).
[2] J. Zhang, X. Wei, I. D. Rukhlenko, H.-T. Chen, and W. Zhu, Electrically tunable metasurface with independent frequency and amplitude modulations, ACS Photonics **7**, 265 (2020).
[3] X. Luo, Subwavelength optical engineering with metasurface waves, Adv. Opt. Mater. **6**, 1701201 (2018).
[4] P. Wu, W.-Y. Tsai, W. Chen, Y.-W. Huang, T.-Y. Chen, J.-W. Chen, C. Liao, C. Chu, G. Sun, and D. Tsai, Versatile polarization generation with an aluminum plasmonic metasurface, Nano Lett. **17**, 445 (2017).
[5] A. A. High, R. C. Devlin, A. Dibos, M. Polking, D. S. Wild, J. Perczel, N. P. De Leon, M. D. Lukin, and H. Park, Visible-frequency hyperbolic metasurface, Nature (London) **522**, 192 (2015).
[6] J. Li, S. Chen, H. Yang, J. Li, P. Yu, H. Cheng, C. Gu, H.-T. Chen, and J. Tian, Simultaneous control of light polarization and phase distributions using plasmonic metasurfaces, Adv. Funct. Mater. **25**, 704 (2015).
[7] K. Koshelev, A. Bogdanov, and Y. Kivshar, Meta-optics and bound states in the continuum, Sci. Bull. **64**, 836 (2019).
[8] S. Jahani and Z. Jacob, All-dielectric metamaterials, Nat. Nanotechnol. **11**, 23 (2016).
[9] Z. Sadrieva, K. Frizyuk, M. Petrov, Y. Kivshar, and A. Bogdanov, Multipolar origin of bound states in the continuum, Phys. Rev. B **100**, 115303 (2019).
[10] K. Koshelev and Y. Kivshar, Dielectric resonant metaphotonics, ACS Photonics **8**, 102 (2021).
[11] U. Fano, Effects of configuration interaction on intensities and phase shifts, Phys. Rev. **124**, 1866 (1961).
[12] A. E. Miroshnichenko, S. Flach, and Y. S. Kivshar, Fano resonances in nanoscale structures, Rev. Mod. Phys. **82**, 2257 (2010).
[13] Y. Yang, I. I. Kravchenko, D. P. Briggs, and J. Valentine, All dielectric metasurface analogue of electromagnetically induced transparency, Nat. Commun. **5**, 5753 (2014).
[14] F. Yesilkoy, E. R. Arvelo, Y. Jahani, M. Liu, A. Tittl, V. Cevher, Y. Kivshar, and H. Altug, Ultrasensitive hyperspectral imaging and biodetection enabled by dielectric metasurfaces, Nat. Photonics **13**, 390 (2019).
[15] J. Jeong, M. D. Goldflam, S. Campione, J. L. Briscoe, P. P. Vabishchevich, J. Nogan, M. B. Sinclair, T. S. Luk, and I. Brener, High quality factor toroidal resonances in dielectric metasurfaces, ACS Photonics **7**, 1699 (2020).
[16] M. Rybin and Y. Kivshar, Supercavity lasing, Nature (London) **541**, 164 (2017).
[17] C. Huang, C. Zhang, S. Xiao, Y. Wang, Y. Fan, Y. Liu, N. Zhang, G. Qu, H. Ji, J. Han *et al.*, Ultra-

fast control of vortex microlasers, Science **367**, 1018 (2020).
[18] S. Liu, P. P. Vabishchevich, A. Vaskin, J. L. Reno, G. A. Keeler, M. B. Sinclair, I. Staude, and I. Brener, An all-dielectric metasurface as a broadband optical frequency mixer, Nat. Commun. **9**, 2507 (2018).
[19] Y. Kivshar, All-dielectric meta-optics and non-linear nanophotonics, Natl. Sci. Rev. **5**, 144 (2018).
[20] J. Von Neumann and E. Wigner, On some peculiar discrete eigenvalues, Phys. Z **30**, 465 (1929).
[21] C. W. Hsu, B. Zhen, A. D. Stone, J. D. Joannopoulos, and M. Soljačić, Bound states in the continuum, Nat. Rev. Mater. **1**, 16048 (2016).
[22] S. Romano, G. Zito, S. Torino, G. Calafiore, E. Penzo, G. Coppola, S. Cabrini, I. Rendina, and V. Mocella, Label-free sensing of ultralow-weight molecules with all-dielectric metasurfaces supporting bound states in the continuum, Photon. Res. **6**, 726 (2018).
[23] D. R. Abujetas, J. Olmos-Trigo, and J. A. Sánchez-Gil, Tailoring accidental double bound states in the continuum in all-dielectric metasurfaces, Adv. Opt. Mater. **10**, 2200301 (2022).
[24] S. Li, C. Zhou, T. Liu, and S. Xiao, Symmetry-protected bound states in the continuum supported by all-dielectric metasurfaces, Phys. Rev. A **100**, 063803 (2019).
[25] A. Kodigala, T. Lepetit, Q. Gu, B. Bahari, Y. Fainman, and B. Kanté, Lasing action from photonic bound states in continuum, Nature (London) **541**, 196 (2017).
[26] M. Wu, S. T. Ha, S. Shendre, E. G. Durmusoglu, W.-K. Koh, D. R. Abujetas, J. A. Sánchez-Gil, R. Paniagua-Domínguez, H. V. Demir, and A. I. Kuznetsov, Room-temperature lasing in colloidal nanoplatelets via Mie-resonant bound states in the continuum, Nano Lett. **20**, 6005 (2020).
[27] A. P. Anthur, H. Zhang, R. Paniagua-Dominguez, D. A. Kalashnikov, S. T. Ha, T. W. W. Maß, A. I. Kuznetsov, and L. Krivitsky, Continuous wave second harmonic generation enabled by quasi bound states in the continuum on gallium phosphide metasurfaces, Nano Lett. **20**, 8745 (2020).
[28] L. Carletti, K. Koshelev, C. De Angelis, and Y. Kivshar, Giant Nonlinear Response at the Nanoscale Driven by Bound States in the Continuum, Phys. Rev. Lett. **121**, 033903 (2018).
[29] K. Koshelev, Y. Tang, K. Li, D.-Y. Choi, G. Li, and Y. Kivshar, Nonlinear metasurfaces governed by bound states in the continuum, ACS Photonics **6**, 1639 (2019).
[30] S. Xiao, M. Qin, J. Duan, F. Wu, and T. Liu, Polarization-controlled dynamically switchable high-harmonic generation from all-dielectric metasurfaces governed by dual bound states in the continuum, Phys. Rev. B **105**, 195440 (2022).
[31] W. Shi, J. Gu, X. Zhang, Q. Xu, J. Han, Q. Yang, L. Cong, and W. Zhang, Terahertz bound states in the continuum with incident angle robustness induced by a dual period metagrating, Photon. Res. **10**, 810 (2022).
[32] T. C. W. Tan, E. Plum, and R. Singh, Lattice-enhanced Fano resonances from bound states in the continuum metasurfaces, Adv. Opt. Mater. **8**, 1901572 (2020).
[33] D. R. Abujetas, Á. Barreda, F. Moreno, A. Litman, J.-M. Geffrin, and J. A. Sánchez-Gil, High-Q transparency band in all-dielectric metasurfaces induced by a quasi bound state in the continuum, Laser Photonics Rev. **15**, 2000263 (2021).
[34] K. Koshelev, S. Lepeshov, M. Liu, A. Bogdanov, and Y. Kivshar, Asymmetric Metasurfaces with High-Q Resonances Governed by Bound States in the Continuum, Phys. Rev. Lett. **121**, 193903 (2018).
[35] W. C. Chew and Q. H. Liu, Perfectly matched layers for elastodynamics: A new absorbing boundary condition, J. Comput. Acoust. **04**, 341 (1996).
[36] T. Wang and G. W. Hohmann, A finite-difference, time-domain solution for three-dimensional electromagnetic modeling, Geophysics **58**, 797 (1993).
[37] D.F. Edwards, in *Handbook of Optical Constants of Solids*, edited by E.D. Palik (Academic, New York, 1997), pp. 547–569.
[38] C. Schinke, P Christian Peest, J. Schmidt, R. Brendel, K. Bothe, M. R. Vogt, I. Kröger, S. Winter, A. Schirmacher, S. Lim *et al.*, Uncertainty analysis for the coefficient of band-to-band absorption of crystalline silicon, AIP Adv. **5**, 067168 (2015).
[39] K. Koshelev, G. Favraud, A. Bogdanov, Y. Kivshar, and A. Fratalocchi, Nonradiating photonics with resonant dielectric nanostructures, Nanophotonics **8**, 725 (2019).
[40] H. M. Doeleman, F. Monticone, W. den Hollander, A. Alù, and A. F. Koenderink, Experimental observation of a polarization vortex at an optical bound state in the continuum, Nat. Photonics **12**, 397 (2018).
[41] L. Cong and R. Singh, Symmetry-protected dual bound states in the continuum in metamaterials, Adv. Opt. Mater. **7**, 1900383 (2019).
[42] A. Krasnok and A. Alú, Low-symmetry nanophotonics, ACS Photonics **9**, 2 (2022).
[43] J. Li, J. Li, C. Zheng, Z. Yue, S. Wang, M. Li, H. Zhao, Y. Zhang, and J. Yao, Free switch between bound states in the continuum (BIC) and quasi-BIC supported by graphene-metal terahertz metasurfaces, Carbon **182**, 506 (2021).
[44] Y. Wang, Z. Han, Y. Du, and J. Qin, Ultrasensitive terahertz sensing with high-Q toroidal dipole resonance governed by bound states in the continuum in all-dielectric metasurface, Nanophotonics **10**, 1295 (2021).
[45] C. W. Hsu, B. Zhen, J. Lee, S.-L. Chua, S. G. Johnson, J. D. Joannopoulos, and M. Soljačić, Observation of trapped light within the radiation continuum, Nature (London) **499**, 188 (2013).
[46] Y. He, G. Guo, T. Feng, Y. Xu, and A. E. Miroshnichenko, Toroidal dipole bound states in the continuum, Phys. Rev. B **98**, 161112(R) (2018).
[47] M.-S. Hwang, H.-C. Lee, K.-H. Kim, K.-Y. Jeong, S.-H. Kwon, K. Koshelev, Y. Kivshar, and H.-G. Park, Ultralow-threshold laser using super-bound states in the continuum, Nat. Commun. **12**, 4135 (2021).
[48] Y. Jahani, E. R. Arvelo, F. Yesilkoy, K. Koshelev, C. Cianciaruso, M. De Palma, Y. Kivshar, and H. Altug, Imaging-based spectrometer-less optofluidic biosensors based on dielectric metasurfaces for detecting extracellular vesicles, Nat. Commun. **12**, 3246 (2021).
[49] H. Altug, S.-H. Oh, S. A. Maier, and J. Homola, Advances and applications of nanophotonic biosensors, Nat. Nanotechnol. **17**, 5 (2022).
[50] Y. Liang, H. Lin, K. Koshelev, F. Zhang, Y. Yang, J. Wu, Y. Kivshar, and B. Jia, Full-Stokes polarization perfect absorption with diatomic metasurfaces, Nano Lett. **21**, 1090 (2021).

[51] V. R. Tuz and A. B. Evlyukhin, Polarization-independent anapole response of a trimer-based dielectric metasurface, Nanophotonics **10**, 4373 (2021).

[52] P. Vaity, H. Gupta, A. Kala, S. Dutta Gupta, Y. S. Kivshar, V. R. Tuz, and V. G. Achanta, Polarization-independent quasi-bound states in the continuum, Adv. Photonics Res. **3**, 2100144 (2022).

[53] L. Yang, S. Yu, H. Li, and T. Zhao, Multiple Fano resonances excitation on all-dielectric nanohole arrays metasurfaces, Opt. Express **29**, 14905 (2021).

[54] X.-S. Li, N. Feng, Y. Xu, Z. Huang, K. Wen, and X. Xiong, Theoretical and simulation study of dynamically tunable sensor based on liquid crystal-modulated Fano resonator in terahertz band, Opt. Laser Technol. **155**, 108350 (2022).

[55] X. Xu, X.-Q. Luo, J. Zhang, W. Zhu, Z. Chen, T.-F. Li, W. M. Liu, and X.-L. Wang, Near-infrared plasmonic sensing and digital metasurface via double Fano resonances, Opt. Express **30**, 5879 (2022).

[56] W. X. Lim, M. Manjappa, Y. K. Srivastava, L. Cong, A. Kumar, K. F. MacDonald, and R. Singh, Ultrafast all-optical switching of germanium-based flexible metaphotonic devices, Adv. Mater. **30**, 1705331 (2018).

[57] G. Li, S. Zhang, and T. Zentgraf, Nonlinear photonic metasurfaces. Nat. Rev. Mater. **2**, 17010 (2017).

[58] V. M. Menon, L. I. Deych, and A. A. Lisyansky, Towards polaritonic logic circuits, Nat. Photonics **4**, 345 (2010).

[59] A. Handelman, I. Lapsker, A. Jacob, and A. Laikhtman, Passive polarized light guiding and thermally induced visible fluorescence in histidine microstructures with optical switching function, Adv. Funct. Mater. **31**, 2008183 (2021).

[60] J. Ou, X.-Q. Luo, Y.-L. Luo, W.-H. Zhu, Z.-Y. Chen, W.-M. Liu, and X.-L. Wang, Near-infrared dual-wavelength plasmonic switching and digital metasurface unveiled by plasmonic Fano resonance, Nanophotonics **10**, 947 (2021).

[61] Y. Luo, X.-Q. Luo, J. Yi, J. Ou, W. Zhu, Z. Chen, W. M. Liu, and X. Wang, Whispering-gallery mode resonance-assisted plasmonic sensing and switching in subwavelength nanostructures, J. Mater. Sci. **56**, 4716 (2021).

[62] I.-C. Benea-Chelmus, S. Mason, M. L. Meretska, D. L. Elder, D. Kazakov, A. Shams-Ansari, L. R. Dalton, and F. Capasso, Gigahertz free-space electro-optic modulators based on Mie resonances, Nat. Commun. **13**, 3170 (2022).

[63] Z. Yu, Y. Wang, B. Sun, Y. Tong, J.-B. Xu, H. K. Tsang, and X. Sun, Hybrid 2D-material photonics with bound states in the continuum, Adv. Opt. Mater. **7**, 1901306 (2019).

[64] E. Melik-Gaykazyan, K. Koshelev, J.-H. Choi, S. S. Kruk, A. Bogdanov, H.-G. Park, and Y. Kivshar, From Fano to quasi-BIC resonances in individual dielectric nanoantennas, Nano Lett. **21**, 1765 (2021).

[65] K. Liu, M. Lian, K. Qin, S. Zhang, and T. Cao, Active tuning of electromagnetically induced transparency from chalcogenideonly metasurface, Light Adv. Manuf. **2**, 251 (2021).

[66] D.-C. Wang, R. Tang, Z. Feng, S. Sun, S. Xiao, and W. Tan, Symmetry-assisted spectral line shapes manipulation in dielectric double-Fano metasurfaces, Adv. Opt. Mater. **9**, 2001874 (2021).

[67] M. Chhowalla, K. B. K. Teo, C. Ducati, N. L. Rupesinghe, G. A. J. Amaratunga, A. C. Ferrari, D. Roy, J. Robertson, and W. I. Milne, Growth process conditions of vertically aligned carbon nanotubes using plasma enhanced chemical vapor deposition, J. Appl. Phys. **90**, 5308 (2001).

[68] C. Vieu, F. Carcenac, A. Pepin, Y. Chen, M. Mejias, A. Lebib, L. Manin-Ferlazzo, L. Couraud, and H. Launois, Electron beam lithography: Resolution limits and applications, Appl. Surf. Sci. **164**, 111 (2000).

[69] G. Zograf, K. Koshelev, A. Zalogina, V. Korolev, R. Hollinger, D.-Y. Choi, M. Zuerch, C. Spielmann, B. Luther-Davies, D. Kartashov *et al.*, High-harmonic generation from resonant dielectric metasurfaces empowered by bound states in the continuum, ACS Photonics **9**, 567 (2022).

[70] J. Wang, J. Kühne, T. Karamanos, C. Rockstuhl, S. A. Maier, and A. Tittl, All-dielectric crescent metasurface sensor driven by bound states in the continuum, Adv. Funct. Mater. **31**, 2104652 (2021).